


 CrossMark
click for updates

 Cite this: *Phys. Chem. Chem. Phys.*,
2016, **18**, 6587

Activated mesoporous carbon nanofibers fabricated using water etching-assisted templating for high-performance electrochemical capacitors†

Geon-Hyoung An, Bon-Ryul Koo and Hyo-Jin Ahn*

Activated mesoporous carbon nanofibers (AMCNFs) are synthesized by a sequential process of electrospinning, water etching-assisted templating, and acid treatment. Their morphologies, crystal structures, melting behavior, chemical bonding states, surface properties, and electrochemical performance are investigated for three different polyacrylonitrile (PAN) to polyvinylpyrrolidone (PVP) weight ratios – PAN:PVP = 8:2, 7:3, and 6:4. Compared to other samples, the AMCNFs with an optimum weight ratio of 6:4 show the highest specific surface area of $692 \text{ m}^2 \text{ g}^{-1}$, a high volume percentage of mesopores of 43.9%, and an increased amount of carboxyl groups (10.5%). This results in a high specific capacitance of 207 F g^{-1} , a high-rate capability with a capacitance retention of 93%, a high energy density of $24.8\text{--}23.1 \text{ W h kg}^{-1}$, and an excellent cycling durability of up to 3000 cycles. The electrochemical performance improvement can be explained by the combined effect of the high surface area relative to the increased electrical double-layers, the high volume fraction of mesopores relative to shorter diffusion routes and low resistance pathways for ions, and the increased amount of carboxyl groups on the CNF surface relative to enhanced wettability.

 Received 4th January 2016,
Accepted 28th January 2016

DOI: 10.1039/c6cp00035e

www.rsc.org/pccp

Introduction

Electrochemical capacitors (ECs) have several advantages over conventional secondary batteries, including a high power density, a fast charge/discharge rate, an excellent cycling durability, and a wide range of operating temperatures.^{1–3} As a result, they are being increasingly used in electric vehicles, portable equipment, large-scale industrial equipment, and memory back-up devices.^{1–3}

ECs can be generally classified into three types according to energy-storage mechanisms: (1) electrical double-layer capacitors (EDLCs) based on a capacitive (non-Faradaic) process using charge separation between the electrolyte and the carbon-based electrode, (2) pseudo-capacitors based on the redox reaction (Faradaic) process using reversible electron-exchange reactions between the electrolyte and the metal-oxide and/or redox polymer-based electrode, (3) hybrid capacitors based on a mixed non-Faradaic and Faradaic process using charge separation at the carbon-based electrode surface and reversible electron-exchange reactions at the metal oxide-based electrode surface.^{4–6} Among the various ECs, EDLCs have been most actively used in industry because of their low fabrication cost, high power density, high-rate capability, and

excellent cycling durability, in spite of their relatively lower specific capacitance when compared to pseudo and hybrid capacitors.^{7–9}

Various carbon-based materials such as activated carbon, carbon nanotubes (CNTs), graphene, and carbon nanofibers (CNFs) have been investigated for use as electrode materials in ECs.^{10,11} Among these, CNFs in particular are extremely suitable as electrode materials in ECs owing to their many advantages that include low cost, large surface areas ($443 \text{ m}^2 \text{ g}^{-1}$), high aspect ratios, low electrical resistance (1.7×10^3), chemical and physical stability, and nanostructure networks for efficient electron transport.^{12–16} To realize high-performance EDLCs, the electrode structure should have a high surface area, high volume percentage of mesopores, high electrical conductivity, and excellent electrochemical stability.^{17,18} A high surface area is the most important factor in achieving the increased capacitance, and the volume percentage of mesopores is important for ensuring a high-rate capability with high specific capacitance retention. Furthermore, high-rate capability is also a very important factor because ECs are generally used in high power devices.^{19–22} Thus, to control the porous structure of CNFs having a high surface area as well as high volume percentage of mesopores, the template strategy is typically used with various inorganic materials such as metals or metal oxides (Sn, SiO_2 , ZnO_2 , CaCO_3 , Al_2O_3 etc.).^{23–27} Inorganic materials embedded in CNFs can form mesopores after the thermal or chemical etching process. For example, An *et al.*¹⁹ used a conventional three-electrode system including mesoporous CNFs prepared by electrospinning followed by Sn segregation with

Department of Materials Science and Engineering,
Seoul National University of Science and Technology, Seoul 139-743, Korea.
E-mail: hjahn@seoultech.ac.kr; Fax: +82-2-973-6657; Tel: +82-2-970-6622

† Electronic supplementary information (ESI) available. See DOI: 10.1039/c6cp00035e

acid etching. The prepared CNFs exhibited a specific surface area of $1082 \text{ m}^2 \text{ g}^{-1}$ and a mesopore volume fraction of 35%, resulting in a high specific capacitance of 289 F g^{-1} at a scan rate of 10 mV s^{-1} . Wang *et al.*²⁶ used self-assembly *via* anodic alumina membranes to prepare mesoporous CNFs having a specific surface area of $698 \text{ m}^2 \text{ g}^{-1}$ and a specific capacitance of 152 F g^{-1} at a scan rate of 5 mV s^{-1} . However, the above-mentioned strategies have drawbacks in commercial application because of their high cost, complexity, time consumption, and acute toxicity (due to the use of hydrofluoric acid).

We therefore synthesized activated mesoporous CNFs with a novel structure using a sequential process of electrospinning, water etching-assisted templating, and acid treatment. The important advantages of using water etching-assisted templating for the successful formation of mesoporous CNFs are low cost, simplicity, quick processing, and mass producibility. We also investigated the relationship between the surface properties and electrochemical behavior of the activated mesoporous CNFs with a high surface area and a high volume percentage of mesopores.

Experimental

Chemicals

Polyacrylonitrile (PAN, $M_w = 150\,000$), polyvinylpyrrolidone (PVP, $M_w = 1\,300\,000$), *N,N*-dimethylformamide (DMF, 99.8%), and nitric acid (70%) were purchased from Sigma-Aldrich. All chemicals were used without further purification.

Synthesis of activated mesoporous carbon nanofibers

We first prepared three different weight ratios of PAN and PVP (PAN/PVP-8:2, PAN/PVP-7:3, and PAN/PVP-6:4, respectively) in DMF under vigorous stirring for 5 h. The mixed total weight of PAN and PVP in DMF was fixed to 10 wt%. For electrospinning, the voltage and the feed rate were maintained at 13 kV and 0.03 mL h^{-1} , respectively. The syringe needle-to-collector distance and humidity in the chamber were set at $\sim 15 \text{ cm}$ and under 10%, respectively. To form the mesoporous structure, the PVP on the as-spun nanofiber (NF) surface was removed by water etching-assisted templating using de-ionized (DI) water in an ultrasonic bath for 0.5 h and then dried in an oven at $80 \text{ }^\circ\text{C}$. The PVP is easily soluble in DI water because of its hydrophilicity. The NFs obtained after selective removal of PVP using DI water were stabilized at $280 \text{ }^\circ\text{C}$ for 2 h in air and then carbonized at $800 \text{ }^\circ\text{C}$ for 2 h under a nitrogen atmosphere (99.999%). To improve the wettability of various mesoporous CNFs, the samples were activated through acid treatment with a HNO_3 solution for 5 h to form oxygen-containing functional groups on the CNF surface, such as C–O, C=O, and O–C=O groups. The resulting samples were washed with DI water several times and dried in an oven at $80 \text{ }^\circ\text{C}$. Thus, we prepared three different types of the activated mesoporous CNFs: AMCNF-8:2, AMCNF-7:3, and AMCNF-6:4. Moreover, for comparison purpose, we also prepared activated CNFs without using the water etching-assisted templating (referred to herein as ACNFs).

Characterization

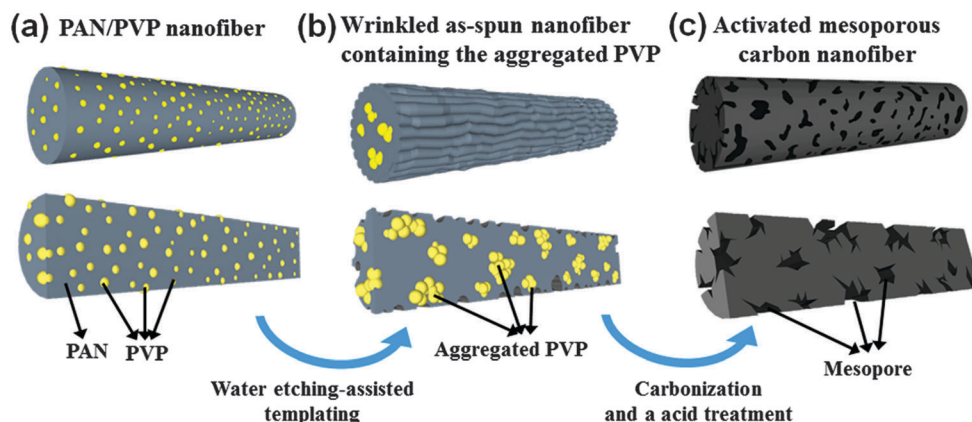
The morphologies and structures of the samples were investigated by field emission-scanning electron microscopy (FE-SEM, Hitachi S-4800) and transmission electron microscopy (MULTI/TEM; Tecnai G², KBSI Gwangju Center). Differential scanning calorimetry (DSC, Shimadzu DSC-60) analyses confirmed the melting behaviors of the as-spun NFs in a temperature range of $30\text{--}500 \text{ }^\circ\text{C}$ under a nitrogen atmosphere at a heating rate of $10 \text{ }^\circ\text{C min}^{-1}$. The crystal structures and chemical bonding states of the samples were characterized by X-ray diffractometry (XRD, Rigaku D/Max 2500 V) with Cu K α radiation in the range from 10° to 90° with a step size of 0.02° and X-ray photoelectron spectroscopy (XPS, ESCALAB250) with an Al K α X-ray source under a base pressure of 267 nPa. The binding energies of each spectrum are standardized to the C 1s core level (284.5 eV). The surface properties such as the specific surface area, pore volume, average pore diameter, and pore volume fraction were characterized by the Brunauer–Emmett–Teller (BET) and Barrett–Joyner–Halenda (BJH) methods using N_2 adsorption at 77 K .

Preparation of electrodes and electrochemical measurements

Electrochemical measurements were performed using a symmetric two-electrode system. The paste, which consists of 80 wt% prepared samples, 10 wt% Ketjen black (Mitsubishi Chemical, ECP-600JD) as a conducting material, and 10 wt% poly(vinylidene difluoride) (PVDF) as a binder in *N*-methyl-2-pyrrolidinone (NMP, 99.5%), was coated on Ni foams of size $1 \text{ cm} \times 1 \text{ cm}$, and the resultant electrodes were dried in air at $100 \text{ }^\circ\text{C}$ for 12 h. The electrolyte used was a 6 M KOH solution. Cyclic voltammetry (CV) measurements were carried out using a potentiostat/galvanostat (Autolab PGSTAT302N, FRA32M) at a scan rate of 10 mV s^{-1} in the potential range of $0.0\text{--}1.0 \text{ V}$. The galvanostatic charging/discharging tests were performed at a current density of $0.2\text{--}10 \text{ A g}^{-1}$ in a voltage range of $0.0\text{--}1.0 \text{ V}$ using a battery cycler system (Won-A Tech., WMPG 3000). The cycling durability of the electrodes was examined at a current density of 1 A g^{-1} up to 3000 cycles.

Results and discussion

Scheme 1 shows a schematic illustration of the AMCNF synthesis process. As shown in Scheme 1a, the as-spun NF consisting of PAN and PVP was prepared by electrospinning. To obtain the mesoporous structures, the PVP on the as-spun NF was removed using DI water in an ultrasonic bath for 0.5 h. During the water etching process, the PVP is easily soluble because of its hydrophilicity, whereas PAN is not soluble because of its hydrophobicity. The resulting as-spun NF surface was therefore wrinkled owing to the removal of PVP from the NF edge surface. Moreover, as shown in Scheme 1b, the residual PVP in the core region causes aggregation owing to the hydrogen bonds in the PVP after ultrasonic treatment. After carbonization at $800 \text{ }^\circ\text{C}$, a mesoporous CNF was formed through decomposition of the aggregated PVP in the core region of the NFs, as shown in Scheme 1c. Finally, an activated mesoporous CNF (Scheme 1c) was formed by acid treatment, which generated oxygen-containing functional groups on the CNF surface.



Scheme 1 A schematic illustration of the AMCNF synthesis process by a sequential process of electrospinning, water etching-assisted templating, and acid treatment.

Fig. 1a–d show FE-SEM images of the as-spun pure PAN NFs, PAN/PVP-8:2, PAN/PVP-7:3, and PAN/PVP-6:4 obtained immediately after electrospinning. All samples exhibit a smooth surface and uniform morphology resulting from the as-spun NFs before calcination. Fig. 1e–h show the pure PAN NFs, PAN/PVP-8:2, PAN/PVP-7:3, and PAN/PVP-6:4 obtained after water etching-assisted templating. Interestingly, as the relative amount of PVP in the NFs increases, the amount of wrinkling of the surface increased from the PAN NFs to PAN/PVP-6:4 gradually owing to the absence of PVP on the NF surface. In other words, the hydrophilic PVP in the NFs is removed by the DI water in the ultrasonic bath, forming the wrinkled as-spun NFs. The hydrophobic PAN in the NFs maintains its

one-dimensional morphology. In particular, of the four samples, PAN/PVP-6:4 has the most wrinkled surface after PVP removal because it contained the largest weight of PVP. Fig. 1i–l present FE-SEM images of ACNFs, AMCNF-8:2, AMCNF-7:3, and AMCNF-6:4 obtained after carbonization at 800 °C. The diameters of all samples with uniform morphology (insets of Fig. 2i–l) are in the range of 191–217 nm. AMCNF-6:4 (Fig. 1l) exhibits a rough surface with large mesopores, implying that a high loading of PVP can result in an increased mesoporous structure due to the selective removal of PVP by water etching-assisted templating.

TEM measurements were performed to further investigate the morphological and structural properties of the samples.

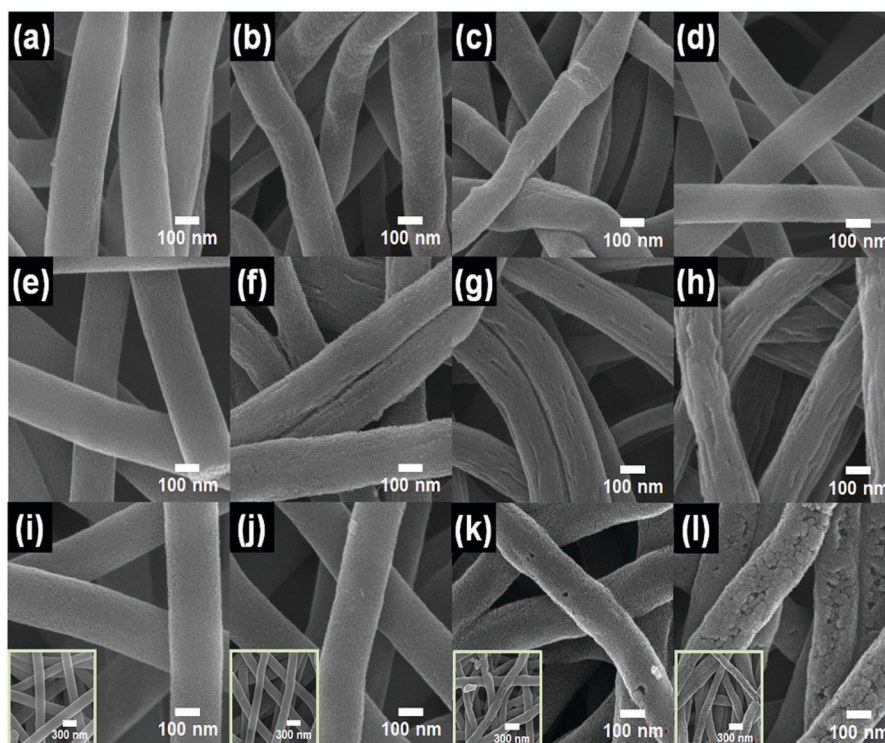


Fig. 1 FE-SEM images of pure PAN NFs, PAN/PVP-8:2, PAN/PVP-7:3, and PAN/PVP-6:4 after electrospinning (a–d) and water etching-assisted templating (e–h). FE-SEM images and inset FE-SEM images of (i) ACNF, (j) AMCNF-8:2, (k) AMCNF-7:3, and (l) AMCNF-6:4.

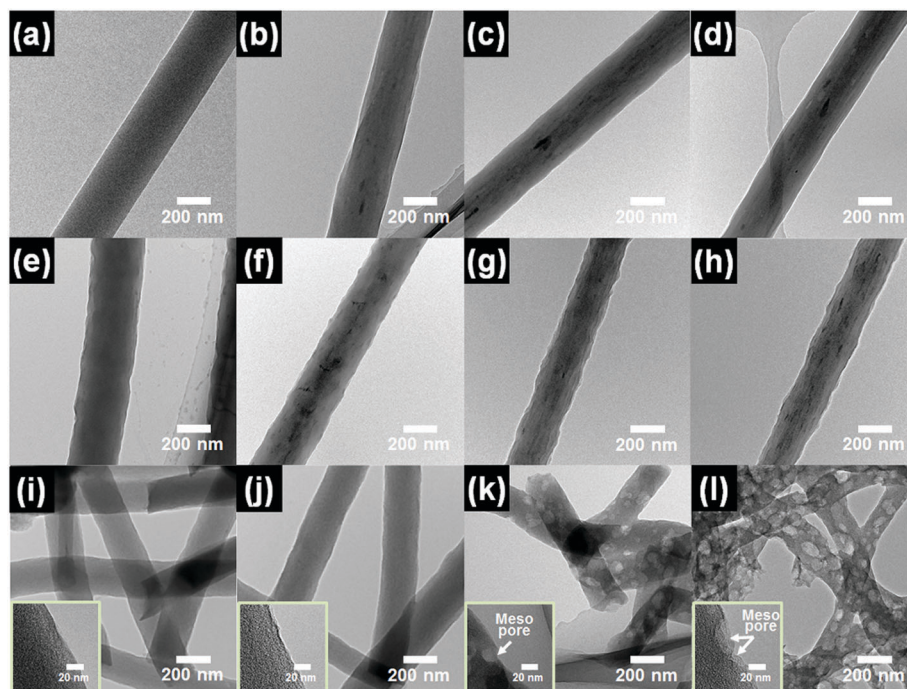


Fig. 2 TEM images of pure PAN NFs, PAN/PVP-8:2, PAN/PVP-7:3, and PAN/PVP-6:4 after electrospinning (a–d) and water etching-assisted templating (e–h). TEM images and inset TEM images of (i) ACNF, (j) AMCNF-8:2, (k) AMCNF-7:3, and (l) AMCNF-6:4.

Fig. 2a–d present TEM images of pure PAN NFs, PAN/PVP-8:2, PAN/PVP-7:3, and PAN/PVP-6:4 obtained immediately after electrospinning. All samples exhibit a uniform contrast owing to the existence of a polymer phase in the NFs with the smooth surface.

Fig. 2e–h present TEM images of the pure PAN NFs, PAN/PVP-8:2, PAN/PVP-7:3, and PAN/PVP-6:4 obtained after water etching-assisted templating. The edge surfaces of PAN/PVP-8:2, PAN/PVP-7:3, and PAN/PVP-6:4 show a relatively brighter contrast than the core region owing to the wrinkled surface, which is in good agreement with SEM results. Fig. 2i–l show TEM images of ACNFs, AMCNF-8:2, AMCNF-7:3, and AMCNF-6:4 after carbonization at 800 °C. AMCNF-6:4, in which most PVP was removed, exhibited a unique porous structure. This implies that the successful formation of mesoporous structures on the CNF surface is mainly attributed to the decomposition of the aggregated PVP in the core region of the NFs. During the water etching process in the ultrasonic bath, the PVP was aggregated in the core region owing to the connection of hydrogen bonds.^{27,28} These results imply that as-spun NFs containing the aggregated PVP in the core region after water etching-assisted templating can directly affect the formation of mesopores in CNFs before carbonization. In addition, the mesopores in ECs can provide a shorter pathway and low resistance for ions at high speeds and high current densities, resulting in high-rate capability with high specific capacitance retention.^{19–22}

To investigate the residual amount of PVP after water etching-assisted templating, DSC analysis was carried out in a temperature range of 30–500 °C under a nitrogen atmosphere, as shown in Fig. 3. For comparison, pure PAN and pure PVP

NFs were prepared by electrospinning. The pure PAN NFs did not indicate melting peaks, but they exhibited a sharp exothermic peak between 239 and 339 °C, corresponding to an oxidative stabilization process.²⁹ The pure PVP NFs showed a melting peak around 85 °C, and thermal decomposition began at around 387 °C.³⁰ The pure PVP NFs have a sharp exothermic peak at 467 °C, corresponding to dehydrogenation due to a loss of hydrogen and oxygen.³⁰ PAN/PVP-8:2, PAN/PVP-7:3, and PAN/PVP-6:4 showed sharp oxidative stabilization peaks of PAN and

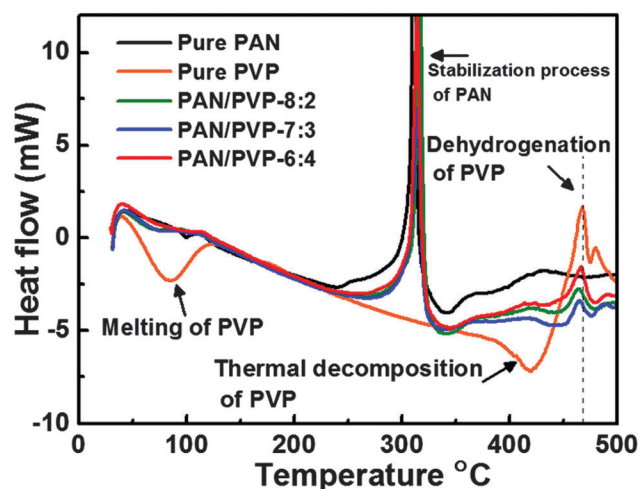


Fig. 3 DSC analysis of pure PAN NFs, PAN/PVP-8:2, PAN/PVP-7:3, and PAN/PVP-6:4 after water etching-assisted templating to investigate the melting behavior in a temperature range of 30–500 °C under a nitrogen atmosphere.

few dehydrogenation peaks of PVP, which implies the existence of residual PVP. PAN/PVP-6:4 exhibited the highest heat flow peak relative to the dehydrogenation of PVP, implying the existence of a large residual amount of PVP in the core region of CNFs. Because PAN is stable in DI water, the PVP existing in the core region may be blocked by the DI water. Therefore, the residual PVP may be located and aggregated in the core region after the water etching process in the ultrasonic bath owing to the connection of hydrogen bonds in the PVP.^{27,28} The large residual amount of PVP could also affect the formation of the mesoporous structure through the dehydrogenation process during the carbonization.^{30,31}

To investigate the surface properties and pore structures, N₂ adsorption/desorption isotherms were examined by BET measurements, as shown in Fig. 4a. The isotherm of ACNF indicates type I characteristics, based on the international union of pure and applied chemistry (IUPAC) nomenclature, implying the presence of microporous pores (of width <2 nm) at relatively low pressures ($P/P_0 < 0.1$).³² In contrast, the isotherm of AMCNF-6:4 exhibits mixed characteristics of types I and IV, which indicates the presence of mesoporous pores (of width 2–50 nm, IUPAC) at an relatively intermediate pressure ($P/P_0 = 0.4$).³² Detailed information on the specific surface area, total pore volumes, average pore diameters, and the pore volume fraction of the samples is summarized in Table 1. The specific surface area of AMCNF-6:4 ($692 \text{ m}^2 \text{ g}^{-1}$) is 1.9, 1.5, and 1.2 times higher than that of the ACNF, AMCNF-8:2, and AMCNF-7:3, respectively. The mesopore volume fraction increases with the amount of PVP. In particular, AMCNF-6:4 exhibits the highest mesopore volume fraction of 43.9%. The mesopore size distribution and mesopore volumes in active materials are known to be important aspects for high-performance ECs at high current density. Fig. 4b presents the BJH analysis for the pore size distributions and pore volumes in the mesopore size range of 2.4–10 nm. AMCNF-6:4 shows the highest mesopore volume in the mesopore size range of 2.4–4.3 nm. The BET and BJH results reveal that AMCNF-6:4 obtained after water etching-assisted templating could be useful in high-performance ECs owing to their high specific capacitance and high-rate capability.

Fig. 5a shows XRD patterns of the samples for investigation of their crystal structures. For all samples, broad diffraction peaks, corresponding to the (002) layers of graphite, are observed at approximately $2\theta = 25^\circ$.³³ These results imply that the crystal structure of ACNFs and AMCNFs is not changed by

Table 1 List of the specific surface area, pore volume, average pore diameter, and pore volume fraction of the ACNF, AMCNF-8:2, AMCNF-7:3, and AMCNF-6:4

Samples	S_{BET} [$\text{m}^2 \text{ g}^{-1}$]	Total pore volume ($P/P_0 = 0.990$) [$\text{cm}^3 \text{ g}^{-1}$]	Average pore diameter [nm]	Pore volume fraction	
				V_{micro} [%]	V_{meso} [%]
ACNF	359	0.18	2.0	84.5	15.5
AMCNF-8:2	460	0.24	2.1	67.7	32.3
AMCNF-7:3	572	0.33	2.3	63.2	36.8
AMCNF-6:4	692	0.45	2.6	56.1	43.9

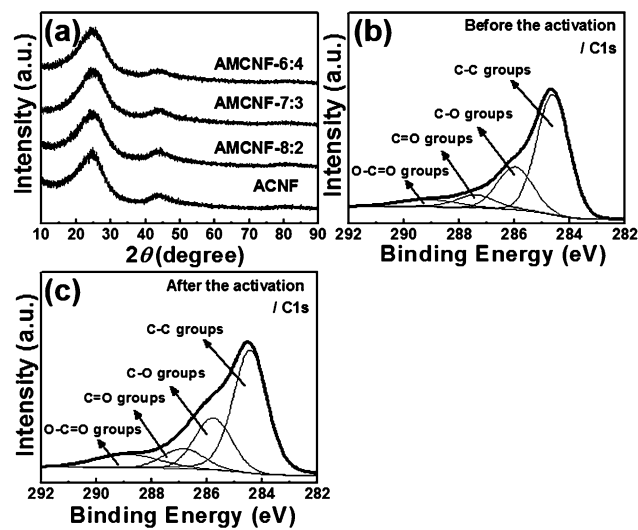


Fig. 5 (a) XRD patterns of ACNF, AMCNF-8:2, AMCNF-7:3, and AMCNF-6:4. XPS spectra of C 1s of AMCNF-6:4 (b) before and (c) after their activation.

the water etching-assisted templating. Moreover, to verify the chemical bonding states of AMCNF-6:4 before and after activation, we performed XPS measurements, as shown in Fig. 5b and c. The results show four peaks, namely C-C at 284.5 eV, C-O at 285.5 eV, C=O at 286.6 eV, and O-C=O at 288.9 eV.³⁴ The O-C=O groups correspond to carboxyl (-COOH) groups and the C-O and C=O groups correspond to hydroxyl (-OH). The percentages of oxygen-containing functional groups on the surface are summarized in Table 2. The percentage of carboxyl groups on AMCNF-6:4 before and after activation was 6.3% and 10.5%, respectively. In other words, there is an increased amount of carboxyl groups on the surface of AMCNF-6:4 after their activation. The increased amount of carboxyl groups on the CNF surface can provide superior electrochemical performance in ECs when compared to carbon-carbon groups because of the improved wettability into an electrolyte that enhances the ion transport capability for improved utilization of the surface area.^{20,22,35}

Fig. 6a shows CV curves of all samples at a scan rate of 10 mV s^{-1} in the potential range of 0.0–1.0 V. The AMCNF-6:4 electrode shows the largest near-rectangular ideal CV curve, which indicates an increased electrical double-layer region resulting from the high specific surface area and high mesopore volume fraction. The specific capacitance (C_{sp}) of all electrodes at a current density

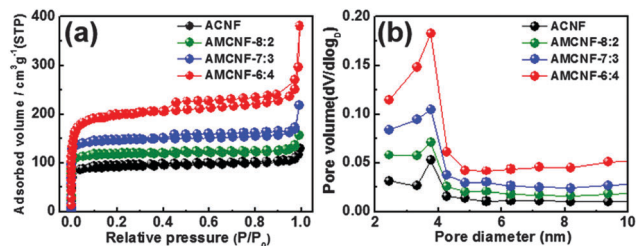


Fig. 4 (a) N₂ adsorption/desorption isotherms and (b) BJH pore size distributions of ACNF, AMCNF-8:2, AMCNF-7:3, and AMCNF-6:4.

Table 2 Percentages of oxygen-containing functional groups on the surface of MCNF-6:4 and AMCNF-6:4 before and after their activation

Samples	C-C (284.5 eV) concentration (%)	C-O (286.0 eV) concentration (%)	C=O (287.4 eV) concentration (%)	O-C=O (288.9 eV) concentration (%)
Before activation	60.8	23.5	9.4	6.3
After activation	56.0	23.6	9.9	10.5

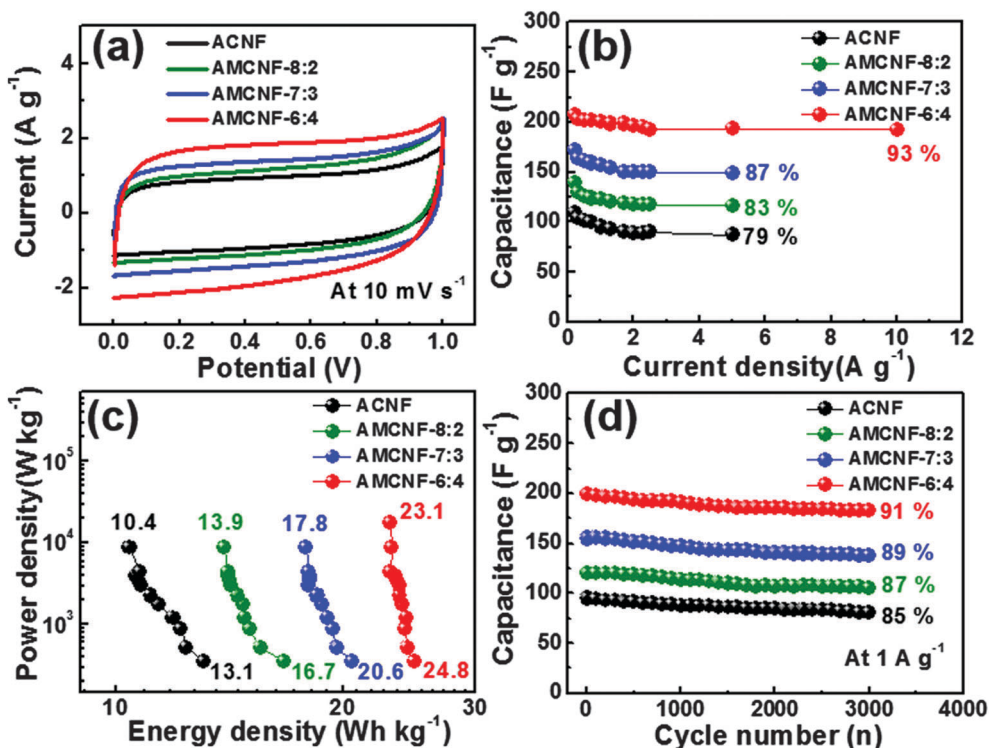


Fig. 6 (a) Cyclic voltammetry (CV) measurements of ACNF, AMCNF-8:2, AMCNF-7:3, and AMCNF-6:4 electrodes at a scan rate of 10 mV s⁻¹ in a voltage range of 0.0–1.0 V. (b) Specific capacitance at a current density of 0.2–10 A g⁻¹. (c) A Ragone plot in the power density range from 349.0–17454.5 W kg⁻¹. (d) Cycling durability at a current density of 1 A g⁻¹ up to 3000 cycles.

of 0.2–10 A g⁻¹ (Fig. 6b) was evaluated according to the following equation:^{36–38}

$$C_{sp} = 4I/(m dV/dt) \quad (1)$$

where I (A) is the charging and discharging current, m (g) is the total mass of the active material, dV is the voltage drop upon discharging, and dt (s) is the total discharging time. The specific capacitances of the ACNF, AMCNF-8:2, AMCNF-7:3, and AMCNF-6:4 electrodes at a current density of 0.2 A g⁻¹ were 109, 139, 171, and 207 F g⁻¹, respectively, as shown in Fig. 6b. The ACNF electrode exhibited a higher specific capacitance of 109 F g⁻¹ than that of a conventional CNF electrode (~44 F g⁻¹, not shown) without activation owing to the increased amount of carboxyl groups on its surface. AMCNF-6:4 showed the highest specific capacitance at all current densities because of its high surface area and the increased amount of carboxyl groups on its surface. However, the MCNF-6:4 electrode without activation indicated a relatively low specific capacitance of 104 F g⁻¹ at a current density of 0.2 A g⁻¹ compared to the AMCNF-6:4 electrode, as observed in Fig. S1 (ESI†). Thus, the carboxyl groups could contribute to enhance the

specific capacitance. As the current density increased, the corresponding specific capacitance reduced slightly owing to the reduced ion diffusion time during the charging/discharging process. Nonetheless, the AMCNF-6:4 electrode showed excellent high-rate capability with a specific capacitance of 192 F g⁻¹ even at a high current density of 10 A g⁻¹ as well as good retention of 93%, which is attributed to the increased mesopore volume fraction of 43.9%. This phenomenon can be explained by the fact that the mesopores on active materials are easily accessible to the ions at a high current density.^{19–22}

In the Ragone plot (Fig. 6c), the energy density (E , Wh kg⁻¹) and power density (P , W kg⁻¹) are calculated based on galvanostatic charging/discharging tests by using the following equation:³⁹

$$E = C_{sp} V^2/8 \quad (2)$$

$$P = E/dt \quad (3)$$

where C_{sp} is the specific capacitance of the two-electrode capacitor, V is the discharging voltage, and dt is the total discharge time. In the Ragone plots, the energy density can be seen to decrease as the

power density is increased. In the case of the ACNF electrode with a low surface area and low mesopore volume fraction, the energy density reduces rapidly as the power density is increased. However, the AMCNF-6:4 electrode shows the highest energy density of 24.8–23.1 W h kg⁻¹ in the power density range from 349–17 454 W kg⁻¹. Fig. 6d shows the cycling durability for all samples measured at a current density of 1 A g⁻¹ up to 3000 cycles. The AMCNF-6:4 electrode showed a superior cycling durability with a specific capacitance retention of 91%. This can be attributed to its high mesopore volume fraction relative to favorable ion diffusion and its improved wettability relative to the efficient utilization of the surface area during the charging and discharging process as well as the nanostructure network of the CNFs with efficient electron transport.^{19,20,22} However, the MCNF-6:4 electrode without activation exhibited relatively poor cycling durability with a specific capacitance retention of 89% compared with the AMCNF-6:4 electrode, as shown in Fig. S2 (ESI†). Thus, the increased amount of carboxyl groups could provide the improved cycling durability due to the efficient utilization of the surface area.

The excellent electrochemical performance of AMCNF-6:4 fabricated by water etching-assisted templating can be attributed to three main effects. First, the high surface area results from the increased capacitance due to the increased contact area between the electrode and the electrolyte. Second, the high mesopore volume fraction results in a high-rate capability and an excellent cycling durability relative to the favorable ion diffusion at a high current density. The favorable ion diffusion is a result of the shorter diffusion routes and low resistance pathways for the ions through the mesopores. Finally, the increased amount of carboxyl groups yielded an excellent cycling durability relative to the enhanced wettability, which resulted from improved utilization of the CNF surface.

Conclusions

Three different types of AMCNFs were synthesized by a sequential process of electrospinning, water etching-assisted templating, and acid treatment. AMCNF-6:4 exhibited a high specific surface area of 692 m² g⁻¹, a total pore volume of 0.41 cm³ g⁻¹, an average pore diameter of 2.6 nm, and a large volume percentage of mesopores of 43.9%. The mesoporous structure mainly resulted from the aggregated PVP in the core region of the NFs. The amount of carboxyl groups (–COOH groups) on the CNF surface increased up to 10.5% after acid treatment. AMCNF-6:4 also exhibited a high specific capacitance of 207 F g⁻¹ at a current density of 0.2 A g⁻¹, a high-rate capability with a capacitance retention of 93%, a high energy density of 24.8–23.1 W h kg⁻¹, and an excellent cycling durability up to 3000 cycles. Therefore, the excellent electrochemical performance of AMCNF-6:4 can be explained by three main aspects: (1) a high surface area relative to the electrical double-layers developed on the surface, (2) a high mesopore volume fraction relative to shorter diffusion routes and low resistance pathways for ions, and (3) an increased amount of carboxyl groups on the surface relative

to the improved utilization of the surface area. These results indicate that AMCNF electrodes have great potential for use in high-performance ECs.

Acknowledgements

This research was supported by Basic Science Research Program through the National Research Foundation of Korea (NRF) funded by the Ministry of Science, ICT and Future Planning (NRF-2015R1A1A1A05001252).

Notes and references

- 1 P. Simon and Y. Gogotsi, *Nat. Mater.*, 2008, **7**, 845–854.
- 2 M. Inagaki, H. Konno and O. Tanaike, *J. Power Sources*, 2010, **195**, 7880–7903.
- 3 J.-Y. Hong, J. J. Wie, Y. Xu and H. S. Park, *Phys. Chem. Chem. Phys.*, 2015, **17**, 30946–30962.
- 4 S. Roldan, D. Barreda, M. Granda, R. Menendez, R. Santamari and C. Blanco, *Phys. Chem. Chem. Phys.*, 2015, **17**, 1084–1092.
- 5 Y. Huang, J. Liang and Y. Chen, *Small*, 2012, **8**, 1805–1834.
- 6 G. Yu, X. Xie, L. Pan, Z. Bao and Y. Cui, *Nano Energy*, 2013, **2**, 213–234.
- 7 M. Kim, I. Oh and J. Kim, *Phys. Chem. Chem. Phys.*, 2015, **17**, 16367–16374.
- 8 R. Liu, L. Pan, L. Wan and D. Wu, *Phys. Chem. Chem. Phys.*, 2015, **17**, 4724–4729.
- 9 J. Zhu, Y. Xu, J. Wang, J. Lin, X. Sun and S. Mao, *Phys. Chem. Chem. Phys.*, 2015, **17**, 28666–28673.
- 10 G.-H. An and H.-J. Ahn, *Ceram. Int.*, 2012, **38**, 3197–3201.
- 11 M.-M. Titirici, R. J. White, N. Brun, V. L. Budarin, D. S. Su, F. Monte, J. H. Clark and M. J. MacLachlan, *Chem. Soc. Rev.*, 2015, **44**, 250–290.
- 12 L. Zhang, A. Aboagye, A. Kelkar, C. Lai and H. Fong, *J. Mater. Sci.*, 2014, **49**, 463–480.
- 13 G.-H. An and H.-J. Ahn, *Electrochem. Solid-State Lett.*, 2014, **3**, M29–M32.
- 14 A. M. Al-Enizi, A. A. Elzatahry, A. M. Abdullah, M. A. AlMaadeed, J. Wang, D. Zhao and S. Al-Deyab, *Carbon*, 2014, **71**, 276–283.
- 15 G.-H. An and H.-J. Ahn, *J. Power Sources*, 2014, **272**, 828–836.
- 16 B.-H. Kim, K. S. Yang, Y. A. Kim, Y. J. Kim, B. An and K. Oshida, *J. Power Sources*, 2011, **196**, 10496–10501.
- 17 P. Cheng, S. Gao, P. Zang, X. Yang, Y. Bai, H. Xu, Z. Liu and Z. Lei, *Carbon*, 2015, **93**, 315–324.
- 18 M. Zhi, C. Xiang, J. Li, M. Li and N. Wu, *Nanoscale*, 2013, **5**, 72–88.
- 19 G.-H. An and H.-J. Ahn, *Carbon*, 2013, **65**, 87–96.
- 20 Q. Li, R. Jiang, Y. Dou, Z. Wu, T. Huang, D. Feng, J. Yang, A. Yu and D. Zhao, *Carbon*, 2011, **49**, 1248–1257.
- 21 B.-H. Kim, K. S. Yang and J. P. Ferraris, *Electrochim. Acta*, 2012, **75**, 325–331.
- 22 J. Lang, X. Yan, W. Liu, R. Wang and Q. Xue, *J. Power Sources*, 2012, **204**, 220–229.
- 23 H. Liu, C.-Y. Cao, F.-F. Wei, Y. Jiang, Y.-B. Sun, P.-P. Huang and W.-G. Song, *J. Phys. Chem. C*, 2013, **117**, 21426–21432.

- 24 L. Ji, Z. Lin, A. J. Medford and X. Zhang, *Carbon*, 2009, **47**, 3346–3354.
- 25 W. Li, F. Zhang, Y. Dou, Z. Wu, H. Liu and X. Qian, *Adv. Energy Mater.*, 2011, **1**, 382–386.
- 26 K. Wang, Y. Wang, Y. Wang, E. Hosono and H. Zhou, *J. Phys. Chem. C*, 2009, **113**, 1093–1097.
- 27 D. Xie, M. Jiang, G. Zhang and D. Chen, *Chem. – Eur. J.*, 2007, **13**, 3346–3353.
- 28 S. Bai, Z. Wang, J. Gao and X. Zhang, *Eur. Polym. J.*, 2006, **42**, 900–907.
- 29 E. Fitzer, W. Frohs and M. Heine, *Carbon*, 1986, **24**, 387–395.
- 30 H. Niu, J. Zhang, Z. Xie, X. Wang and T. Lin, *Carbon*, 2011, **49**, 2380–2388.
- 31 T. Le, Y. Yang, Z. Huang and F. Kang, *J. Power Sources*, 2015, **278**, 683–692.
- 32 G.-H. An, H.-J. Ahn and W.-K. Hong, *J. Power Sources*, 2015, **274**, 536–541.
- 33 G.-H. An, S.-J. Kim, K.-W. Park and H.-J. Ahn, *Electrochem. Solid-State Lett.*, 2014, **3**, M21–M23.
- 34 A. P. Terzyk, *Colloids Surf., A*, 2001, **177**, 23–45.
- 35 C. Ma, Y. Li, J. Shi, Y. Song and L. Liu, *Chem. Eng. J.*, 2014, **249**, 216–225.
- 36 X. Li, W. Xing, S. Zhuo, J. Zhou, F. Li, S.-Z. Qiao and G.-Q. Lu, *Bioresour. Technol.*, 2011, **102**, 1118–1123.
- 37 M. Liu, W. W. Tjiu, J. Pan, C. Zhang, W. Gao and T. Liu, *Nanoscale*, 2014, **6**, 4233–4242.
- 38 G.-H. An and H.-J. Ahn, *J. Electroanal. Chem.*, 2015, **744**, 32–36.
- 39 X. Yang, L. Zhang, F. Zhang, T. Zhang, Y. Huang and Y. Chen, *Carbon*, 2014, **72**, 381–386.